A discrete dual finite volume method for the steady-state advection-diffusion-reaction equation

Thomas Bonnafont[1], Delphine Bessières[2], and Jean Paillol[2]

[1]*Lab-STICC, CNRS UMR 6285, ENSTA, Institut Polytechnique de Paris, Brest, France*

[2]*Université de Pau et des Pays de l'Adour, E2S UPPA, SIAME, Pau France*

November 28, 2025

Abstract

This paper presents an extension of the discrete dual finite volume (DDFV) method to solve the stationary advection-diffusion-reaction equation with mixed boundary conditions. As a particular case, we also consider the Helmholtz equation with absorbing boundary conditions. The main point is to propose a self-consistent method where the advection term is also discretized in the primal/dual mesh of DDFV. Here, we propose two different approximations of the advection term using the primal/dual mesh. In addition, we also derive an exponential fitted DDFV scheme to compare them in terms of accuracy and conditioning. A major advantage of DDFV is its ability to naturally handle diffusion terms while preserving fundamental mathematical properties such as Green's identity. This makes the implementation of Robin boundary conditions straightforward. However, treating the advection term requires additional considerations. We achieve this by approximating the normal gradient using the discrete DDFV gradient and adjusting the corresponding matrix terms accordingly. To validate our approach, we establish the existence of solutions for the discrete schemes and conduct numerical experiments on both the advection-diffusion-reaction and Helmholtz equations. The results confirm that our method exhibits second-order superconvergence in general, even when applied to highly distorted meshes, demonstrating its robustness and accuracy.

1 Introduction

In this work, we study the steady advection-diffusion-reaction equation, given by

$$-\nabla \cdot (\mu \nabla q) + \nabla \cdot (\mathbf{V} q) + \gamma q = f, \quad \text{in } \Omega, \tag{1}$$

where q is the quantity of interest, μ the diffusion tensor, $\mathbf{V}$ a vector field representing the particle velocity, γ the reaction coefficient, and f a source term. This equation is completed with mixed boundary conditions applied on subsets Γ_{N}, Γ_{D}, and Γ_{R} of the domain boundary, corresponding to Neumann, Dirichlet, and Robin conditions.

Our main objective is to develop a self-consistent *discrete dual finite volume* (DDFV) scheme [1, 2, 3, 4, 5] to solve (1) under mixed boundary conditions. Efficient numerical schemes for (1) are crucial for various applications, particularly in electromagnetism. When $\mathbf{V} = 0$, the equation reduces to the Helmholtz equation, which models wave propagation (acoustic or electromagnetic) in the frequency domain [6]. In addition, a reaction term γq can also appear when an exponential fitting procedure is applied to the advection-diffusion equation [7, 8, 9, 10]. Moreover, the unsteady counterpart of (1), coupled with a Poisson equation, arises in modeling cold plasma [11], electrostatic discharges [12, 13], and electroporation phenomena [14].

Traditional finite volume methods (FVM) [15, 16]—such as the two-point flux approximation—are widely used due to their reduced stencil and local flux approximation at mesh interfaces. However, they require an admissible mesh satisfying orthogonality constraints [17], limiting their applicability to complex geometries. Finite difference methods also face challenges on irregular meshes, often

necessitating advanced techniques like ghost points or immersed interfaces [18, 19, 20] for handling interface conditions.

More recently, *mimetic schemes* have shown promising results [21, 22, 23]. Indeed, they allow us to build a scheme that preserves physical or mathematical properties, such as the Green relation. This work focuses on the DDFV scheme [24, 16], which is a mimetic finite volume method. In a few words, DDFV is based on a well-defined diamond mesh, allowing us to recover a discrete Green relation while no orthogonal constraints on the mesh are required. Furthermore, as for usual finite volume schemes, jump conditions are easily accounted for [2, 5]. Additionally, DDFV offers strong convergence properties, achieving a second-order super-convergence rate even on highly distorted meshes, while first-order accuracy has been shown [2, 3, 24] in general.

DDFV has been successfully applied to Poisson's equation [1, 25, 26, 2, 27, 5] and steady convection-diffusion problems [24]. It has also been used for the Navier-Stokes equation [28, 29, 30], the Stokes equation [31, 32, 33, 34], and for transport-diffusion equations [35, 36, 37, 4, 38], where WENO schemes were employed for transport fluxes. In this work, we extend the approach in [24] to the advection-diffusion-reaction equation while incorporating mixed boundary conditions. Contrary to [37], no WENO interpolation scheme is used and only the DDFV unknowns are utilized, leading to a self-consistent scheme. Also, we differentiate from [24] by proposing a new approximation of the advection term using the primal/dual coupling of the DDFV scheme. By leveraging the discrete Green property of DDFV, we show that Neumann and Robin conditions are naturally handled. In addition, we also present an exponential fitting procedure, as in [10], that allows for a change of variable to solve a diffusion equation in place of the advection-diffusion equation, leading to a direct use of the efficient DDFV scheme and to overcome the non-coercivity problem for certain values of $\mathbf{V} \cdot \mathbf{n}$. As a special case, we examine the Helmholtz equation ($\mathbf{V} = 0$) and demonstrate how the proposed scheme efficiently manages absorbing boundary conditions, making it well-suited for modeling electromagnetic wave propagation in the frequency domain. To the authors' knowledge, the DDFV scheme has not yet been applied to the steady-state advection-diffusion-reaction with mixed boundary conditions, and has not been generalized to the case of the Helmholtz equation where we seek $q \in \mathbb{C}$.

The rest of the paper is organized as follows. Section 2 is devoted to describing the problem in more detail and introducing the DDFV scheme to solve the advection-diffusion-reaction equation. In Section 3, numerical experiments are performed to validate the method. In particular, we study the advection-diffusion-reaction and the Helmholtz equations under mixed boundary conditions (Dirichlet, Neumann, and Robin). Finally, Section 4 concludes the paper and gives perspective for future works.

2 Description of the computational scheme

2.1 Definition of the problem and notations

In this work, we will either work in $\mathbb{R}$ and $\mathbb{C}$ depending on the application. In particular, when studying the Helmholtz equation for electromagnetic wave propagation, then $\gamma \in \mathbb{C}$. Therefore, we will use the notation $\mathbb{K}$ for either $\mathbb{R}$ or $\mathbb{C}$. In the case of $\mathbb{C}$, we denote by $\overline{q}$ the complex conjugate of q, and by $\Re(q)$ and $\Im(q)$ its real and imaginary parts. Furthermore, we restrict our case to problems in $\mathbb{R}^2$, such that $\Omega \subset \mathbb{R}^2$. We denote its boundary by $\partial\Omega$. The latter can be decomposed into $\Gamma_{\mathrm{D}} \cup \Gamma_{\mathrm{N}} \cup \Gamma_{\mathrm{R}}$ for the Dirichlet, Neumann, and Robin boundary conditions, respectively. Furthermore, the vectors are denoted in bold as $\mathbf{V}$, and their normalized counterparts in lowercase as $\mathbf{v}$. Throughout the paper, we also denote by ∂_n the normal gradient defined as $\partial_n u = \nabla u \cdot \mathbf{n}$ with $\mathbf{n}$ the exterior normal to the considered interface.

As said in the introduction, we are interested in solving the following general problem

$$\left\{\begin{array}{rcll} -\nabla \cdot (\mu \nabla q) + \nabla \cdot (\mathbf{V} q) + \gamma q & = & f, & \text{in } \Omega, \\ q & = & g^{\mathrm{D}}, & \text{on } \Gamma_{\mathrm{D}}, \\ \mu \partial_n q & = & g^{\mathrm{N}}, & \text{on } \Gamma_{\mathrm{N}}, \\ \mu \partial_n q + \beta q & = & g^{\mathrm{R}}, & \text{on } \Gamma_{\mathrm{R}}, \end{array}\right. \tag{2}$$

where $\mu \in \mathbb{K}$ the diffusion coefficient, such that $\mu_* \leq \mu \leq \mu^*$ with $\mu_* > 0$ almost everywhere in Ω, $\mathbf{V} \in (L^\infty(\Omega))^2$ and $\nabla \cdot \mathbf{V} \in L^\infty(\Omega)$, $\gamma \in \mathbb{K}$ the reaction coefficient, $f \in L^2(\Omega)$, β a constant in $\mathbb{K}$ and $g^{\mathrm{i}} \in H^{1/2}(\partial\Omega)$. In this case, under some mild assumptions [39, Chapter 3], problem (2) admits $q \in H^1(\Omega)$ as a weak solution. Note that in the case of the Helmholtz equation, i.e., $\mathbf{V} = 0$, $\mu = 1$ and

$\gamma \in \mathbb{C}$ of the same sign as the diffusion coefficient, then the proof relies on $\Im(\gamma) > 0$, where $\Im$ is the imaginary part. When an exponential fitting [7, 8] is performed to handle the advection term, then the reaction term $\gamma \in \mathbb{R}$, and $\gamma\mu \leq 0$, leading to direct coercivity of the operator.

2.2 The DDFV diamond mesh

As mentioned in the introduction, the DDFV scheme relies on a diamond mesh constructed from a primal/dual mesh pairing. This section introduces this pair and the derived diamond mesh.

The *primal mesh*, denoted by $\mathcal{P}_h$, consists here of a standard conformal quadrangular partition of the domain Ω. Each control volume $\mathcal{K} \in \mathcal{P}_h$ has a center denoted by $x_\mathcal{K}$. The interface between two adjacent primal cells $\mathcal{K} \in \mathcal{P}_h$ and $\mathcal{L} \in \mathcal{P}_h$ is denoted by ν. An example of a primal mesh is given in Figure 1 (a), where the green points denote the center of each control volume and the filled ones the center at the domain's boundary.

We directly derive the *dual mesh* from this primal mesh, denoted by $\mathcal{P}_h^*$. Indeed, here each primal vertex serves as the center of a dual control volume $\mathcal{K}^* \in \mathcal{P}_h^*$. Conversely, the vertices of $\mathcal{K}^*$ correspond to the centers of adjacent primal control volumes $\mathcal{K}$. The center of a dual control volume is denoted by $x_{\mathcal{K}^*}$. Furthermore, considering two adjacent dual cells $\mathcal{K}^*$ and $\mathcal{L}^*$, we denote by ν^* their interface. This construction is illustrated in Figure 1 (b), where the squares correspond to the dual center and the filled ones are dual centers at the boundary of the domain.

The complete partition of the domain Ω is then denoted by $\mathcal{T}_h$ such that $\mathcal{T}_h = \mathcal{P}_h \cup \mathcal{P}_h^*$. The latter is an overlapping partition of Ω.In addition, we denote by $\partial\mathcal{T}_h$ its boundary interfaces, that can be decomposed into $\partial\mathcal{T}_h^\mathrm{D} \cup \partial\mathcal{T}_h^\mathrm{N} \cup \partial\mathcal{T}_h^\mathrm{R}$ to account for the different boundaries. The discrete counterpart of the unknown q in $\mathcal{T}_h$ is denoted by $q^{\mathcal{T}_h}$ such that $q^{\mathcal{T}_h} = (q_{\mathcal{K}\in\mathcal{P}_h}, q_{\mathcal{K}^*\in\mathcal{P}_h^*}) \in \mathbb{K}^{\mathcal{T}_h}$.

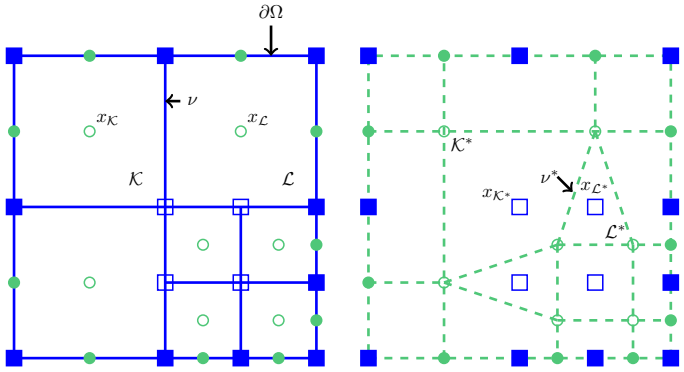

(a) Primal mesh $\mathcal{P}_h$ (b) Dual mesh $\mathcal{P}_h^*$

Figure 1: Example of the primal and dual meshes when a quadrangular grid is considered. The circle corresponds to the primal unknowns, while the square indicates the dual ones. The filling indicates boundary unknowns.

We can now define the *diamond mesh* denoted as $\mathcal{D}_h$. Let us consider two adjacent primal (or dual) cells $\mathcal{K}$ and $\mathcal{L}$ that share the common edge $\nu = [x_{\mathcal{K}^*} x_{\mathcal{L}^*}]$, where $\mathcal{K}^*$ and $\mathcal{L}^*$ are the associated dual cells. Then each diamond is defined as the quadrangle $\mathcal{D} = [x_\mathcal{K} x_{\mathcal{K}^*} x_\mathcal{L} x_{\mathcal{L}^*}] \in \mathcal{D}_h$. One example is given in Figure 2. Additionally, we denote by $\mathbf{N}_\nu$ and $\mathbf{N}_{\nu^*}$ the normals to the edges ν and ν^*, respectively. When needed, their normalized counterpart are denoted in lower case, e.g. $\mathbf{n}_\nu$ and $\mathbf{n}_{\nu^*}$. This structure establishes a direct link between $\mathcal{P}$ and $\mathcal{P}^*$ and is at the core of the mimetic structure of DDFV.

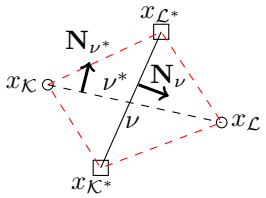

Figure 2: An example of a diamond $\mathcal{D}$ of the set of diamonds $\mathcal{D}_h$.

Finally, we define some useful spaces and scalar products in our discrete setting. First, let us define $L^2(\mathcal{D}_h)$, the set of discrete vector fields over $\mathcal{T}_h$ and piecewise constant in $\mathcal{D}_h$. The latter is equipped, as a subset of $L^2(\Omega)$, with the following scalar product [40]

$$\forall \psi, \phi \in L^2(\mathcal{D}_h),\ (\psi, \phi)_{L^2(\mathcal{D}_h)} = \sum_{\sigma \in \mathcal{S}} \phi_\sigma \cdot \overline{\psi}_\sigma |\mathcal{D}|, \tag{3}$$

with $|\mathcal{D}|$ the measure of the corresponding diamond, and $\mathcal{S}$ the set of interfaces, i.e., the boundaries of either $\mathcal{K}$ for the primal or $\mathcal{K}^*$ for the dual. Second, we define $L^2(\partial\mathcal{T}_h)$ consisting of the functions defined on $\partial\Omega$ that are piecewise constant for $\sigma \in \partial\mathcal{T}_h$. This set is equipped with the following inner product

$$\forall \psi, \phi \in L^2(\partial\mathcal{T}_h),\ (\psi, \phi)_{L^2(\partial\mathcal{T}_h)} = \sum_{\sigma \in \partial\mathcal{T}_h} \phi_\sigma \cdot \overline{\psi}_\sigma |\sigma|. \tag{4}$$

To conclude, the finite volume approximation of ϕ is defined as usual by

$$\tilde{\phi} = \frac{1}{|\mathcal{T}|} \int_{\mathcal{T}} \phi.$$

We also define as $\mathcal{F}(\mathcal{T}_h)$ the set of these functions over $\mathcal{T}_h$, and by $P^1(\mathcal{T}_h)$ the set of differentiable finite volume functions. Thus, we can define the following bracket [40]

$$\forall \phi \in \mathcal{F}(\mathcal{T}_h), \psi \in P^1(\mathcal{T}_h),\ \langle \phi, \psi \rangle_{\mathcal{F}(\mathcal{T}_h) \times P^1(\mathcal{T}_h)} = \frac{1}{2} \left(\sum_{\mathcal{K} \in \mathcal{P}_h} \phi_\mathcal{K} \overline{\psi}(x_\mathcal{K}) |\mathcal{K}| + \sum_{\mathcal{K}^* \in \mathcal{P}_h^*} \phi_{\mathcal{K}^*} \overline{\psi}(x_{\mathcal{K}^*}) |\mathcal{K}^*| \right) \tag{5}$$

2.3 Definition of the discrete operators

Then, to discretize Equation (1), we must define the proper discrete counterpart of each operator, i.e., the advection and the diffusion ones here.

2.3.1 The discrete diffusion operator

Let us begin with the diffusion operator, which is the easiest of the two. Indeed, in this case, we can directly follow the DDFV scheme that solves the Poisson equation [2, 3, 5] and utilize the discrete gradient and divergence operators' definitions.

Definition 2.1 (Discrete gradient ∇_h)**.** First, let us define the discrete gradient operator $\nabla_h : P^1(\mathcal{T}_h) \mapsto L^2(\mathcal{D}_h)$ as

$$\nabla_h q^{\mathcal{T}_h} = \frac{1}{2|\mathcal{D}|} \left((q_\mathcal{L} - q_\mathcal{K}) \mathbf{N}_\nu + (q_{\mathcal{L}^*} - q_{\mathcal{K}^*}) \mathbf{N}_{\nu^*} \right), \tag{6}$$

with $|\mathcal{D}|$ the measure of the diamond $\mathcal{D} = [x_K x_{K^*} x_L x_{L^*}]$.

Proof. The proof that (6) corresponds to the discrete gradient of $q^{\mathcal{T}_h}$ has been given in [40], for example. It is quite direct using the fact that $q^{\mathcal{T}_h}$ is affine on each simplex of the diamond and using the gradient theorem. □

Next, we can define the discrete divergence operator $\mathrm{div}^{\mathcal{T}_h} : L^2(\mathcal{D}_h) \mapsto \mathcal{F}(\mathcal{T}_h)$ that links back the diamond mesh to the $\mathcal{T}_h$ mesh.

Definition 2.2 (Discrete divergence operator $\mathrm{div}^{\mathcal{T}_h}$)**.** The discrete divergence operator $\mathrm{div}^{\mathcal{T}_h}$ is defined as follows

$$\begin{aligned} \forall \mathcal{K} \in \mathcal{P},\ \forall \xi^D \in L^2(\mathcal{D}_h), \quad \mathrm{div}_\mathcal{K}^{\mathcal{T}_h}\left(\xi^D\right) &= \frac{1}{|\mathcal{K}|} \textstyle\sum_{\nu \in \mathcal{D}_\mathcal{K}} \xi^D \cdot \mathbf{N}_\nu, \\ \forall \mathcal{K}^* \in \mathcal{P}^*,\ \forall \xi^D \in L^2(\mathcal{D}_h), \quad \mathrm{div}_{\mathcal{K}^*}^{\mathcal{T}_h}\left(\xi^D\right) &= \frac{1}{|\mathcal{K}^*|} \textstyle\sum_{\nu^* \in \mathcal{D}_{\mathcal{K}^*}} \xi^D \cdot \mathbf{N}_{\nu^*}, \end{aligned} \tag{7}$$

where $|\cdot|$ corresponds to the measure of the control volume, and $\mathcal{D}_\mathcal{K}$ (or $\mathcal{D}_{\mathcal{K}^*}$) to the diamonds associated to the $\mathcal{K}$ (or $\mathcal{K}^*$) cell. For example, in our quadrangular mesh, for each inner control volume we have 4 diamonds to account for.

Proof. The proof for (7) has also been given in [1, 40], for example, and relies on the application of the Green formula for the diffusion operator on each control volume. □

To properly define the quantities on $\partial\Omega$ and the discrete counterpart of the Green formula, we first need to define a discrete trace operator.

Definition 2.3 (Discrete trace operator Tr_h)**.** Let us denote by $\partial\mathcal{T}_h$ the set of boundary interfaces. Then the discrete trace operator $\mathrm{Tr}_h : P^1(\mathcal{T}_h) \mapsto L^2(\partial\mathcal{T}_h)$ is defined as

$$\mathrm{Tr}_h(q) = \frac{1}{2} q_\sigma + \frac{1}{4}\left(q_{\sigma_1^*} + q_{\sigma_2^*}\right), \tag{8}$$

where q_σ is the value at the center of the boundary simplex, and $q_{\sigma_1^*}$ and $q_{\sigma_2^*}$ are the values at its vertices.

Proof. We derive the proof as in [40]. The trace operator is defined as

$$\mathrm{Tr}(q) = \frac{1}{|\sigma|}\int_\sigma q(s)ds.$$

Thus, using the fact that q is affine on the simplex σ, we directly obtain formula (8). □

Furthermore, DDFV is a mimetic finite volume scheme where the discrete gradient (6) and the discrete divergence (7) are linked throughout a discrete Green formula [1, 40, 2].

Definition 2.4 (Discrete Green formula)**.** On the discrete mesh $\mathcal{T}_h$, we have the following duality formula between the discrete gradient and divergence

$$\left\langle \mathrm{div}^{\mathcal{T}_h}(\xi^D), \psi \right\rangle_{\mathcal{F}(\mathcal{T}_h)\times P^1(\mathcal{T}_h)} = -(\xi^D, \nabla_h\psi)_{L^2(\mathcal{T}_h)} + (\xi^D\cdot\mathbf{n}, \mathrm{Tr}_h\psi)_{L^2(\partial\mathcal{T}_h)}. \tag{9}$$

Proof. For the interested reader, the proof is given in [1, 40], for example. □

2.3.2 The discrete advection operator

Now, let us focus on the convection operator. A key challenge here is that we cannot directly use the discrete divergence $\mathrm{div}^{\mathcal{T}_h}$ or the discrete gradient ∇_h, as they do not map quantities within $\mathcal{T}_h$. To address this, we adopt an upwind standard finite volume strategy for the convection operator, while ensuring consistency with the DDFV scheme by working within the mesh $\mathcal{T}_h$.

Definition 2.5 (Discrete advection operator $\nabla\cdot(\mathbf{V}q)^{\mathcal{T}_h}$)**.** The discrete advection operator maps quantities from $P^1(\mathcal{T}_h)$ to $\mathcal{F}(\mathcal{T}_h)$ and is defined as

$$\forall\mathcal{T}\in\mathcal{T}_h,\ \nabla\cdot(\mathbf{V}q)_{\mathcal{T}}^{\mathcal{T}_h} = \frac{1}{|\mathcal{T}|}\sum_{\sigma\in\partial\mathcal{T}} q(x_\sigma)(\mathbf{V}(x_\sigma)\cdot\mathbf{N}_\sigma), \tag{10}$$

with x_σ the point at the middle of the simplex $\sigma\in\partial\mathcal{T}$.

Proof. To obtain the discrete form of the operator, we start by integrating the convection term over a control volume $\mathcal{T}\in\mathcal{T}_h$ and applying the divergence theorem, yielding

$$\int_{\mathcal{T}}\nabla\cdot(\mathbf{V}q) = \sum_{\sigma\in\partial\mathcal{T}}\int_\sigma q(x)(\mathbf{V}(x)\cdot\mathbf{n}_\sigma)dx, \tag{11}$$

where $\partial\mathcal{T}$ denotes the boundary of the control volume $\mathcal{T}$, and $\mathbf{n}_\sigma$ represents its outward normal. Finally, using the fact that q is affine on each simplex of $\mathcal{T}_h$ we obtain the desired result (10). □

Nonetheless, the quantity $q(x_\sigma)$ is not defined in $\mathcal{T}_h$, thus, we need to approximate it using the DDFV unknowns. Since upwinding is required to account for the advection term [41] precisely, we use the following approximations.

Definition 2.6. Approximating $q(x_\sigma)$ For a first-order method, we approximate the value of q at the interface using

$$q(x_{\sigma_i}) = q(x_{\mathcal{T}^\pm}), \tag{12}$$

where $q(x_{\mathcal{T}^\pm})$ corresponds to the value at the center of the control volume $\mathcal{T}^\pm \in \mathcal{T}_h$, where the $\pm$ denote the side of σ, which depends on the flux direction. However, to maintain second-order accuracy, following the DDFV scheme, we employ the following second-order approximation:

$$q(x_{\sigma_i}) = q(x_{\mathcal{T}^\pm}) + \nabla_{\mathcal{T}_h} q(x_{\mathcal{T}^\pm}) \cdot (x_{\mathcal{T}^\pm} - x_\sigma), \tag{13}$$

where $\nabla_{\mathcal{T}_h}$ is an appropriately defined gradient on $\mathcal{T}_h$. We can also derive a second-order accurate scheme using the following approximation

$$q(x_{\sigma_i}) = \frac{1}{2}(q(x^1_{\sigma_i}) + q(x^2_{\sigma_i})), \tag{14}$$

with $\sigma_i = [x^1_{\sigma_i}, x^2_{\sigma_i}]$. Note that the latter directly uses the coupling between the primal and dual meshes. Furthermore, no conditions on the flux are needed.

It shall be noted a different strategy has been proposed in [42] to account for the advection using DDFV unknowns. Even if the idea seems similar, they used the primal unknowns for the linear interpolation, which only works if the dual interfaces are continuous which is usually not the case with very distorted meshes.

In the following, we only use the 2nd order schemes and will denote by DDFV and iDDFV the ones derived from (13) and (14), respectively.

Proof. The result is direct considering Taylor expansions, as seen in [24] and the fact that we are using an upwind scheme. Indeed, in this case, if the flux, i.e., $\mathbf{V} \cdot \mathbf{n}_\sigma$, is of positive sign, then $x_{\mathcal{T}^\pm} = x_\mathcal{K}$ (or $x^*_\mathcal{K}$), which is on the left side of σ, while $x_{\mathcal{T}^\pm} = x_\mathcal{L}$ (or $x^*_\mathcal{L}$) in the case of a negative flux. Obtaining the approximation of equation (14) is also direct since q is affine on each simplex[1]. □

To introduce this gradient more intuitively, consider a quadrangular control volume $\mathcal{T} \in \mathcal{T}_h$, illustrated in Figure 3. The center of the cell, denoted by x_T, may correspond to either a primal or dual volume, while its vertices correspond to the centers of the respective dual or primal cells. Using these four points, we define the discrete gradient as follows.

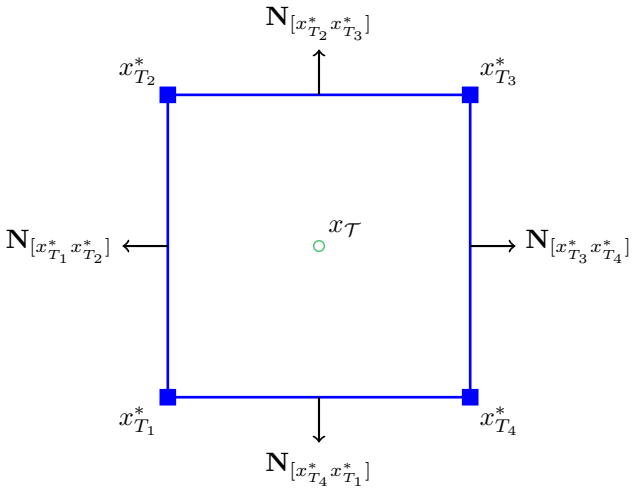

Figure 3: Example of a control volume $\mathcal{T}$ with its center $x_\mathcal{T}$ and its four dual centers denoted with a * superscript.

[1] Note that if $\mathbf{V}$ is constant, we could also derive it directly from $\nabla \cdot (\mathbf{V}q) = \mathbf{V} \cdot \nabla q$ and the approximation of the gradient.

Definition 2.7 (Discrete gradient $\nabla_{\mathcal{T}_h}$)**.** The discrete gradient $\nabla_{\mathcal{T}_h} : P^1(\mathcal{T}_h) \mapsto \mathcal{F}(\mathcal{T}_h)$ is defined by

$$\nabla_{\mathcal{T}_h} q^{\mathcal{T}_h} = \frac{1}{|\mathcal{T}|} \sum_{i=1}^{4} \frac{q(x^*_{T_i}) + q(x^*_{T_{i+1}})}{2} \mathbf{N}_{[x^*_{T_i} x^*_{T_{i+1}}]}, \tag{15}$$

where T_i corresponds to the vertices of $\mathcal{T}$, such that $x^*_{T_5} = x^*_{T_1}$ ensures periodic indexing for our quadrangular grid, $\mathbf{N}_{[x^*_{T_i} x^*_{T_{i+1}}]}$ is the outward normal to the segment $[x^*_{T_i} x^*_{T_{i+1}}]$, and $|\mathcal{T}|$ denotes the measure of the control volume.

Proof. The proof follows directly from the gradient theorem and that q is affine on each simplex of $\mathcal{T} \in \mathcal{T}_h$. □

Furthermore, on the entire domain, this gradient can be efficiently computed using a loop over the diamonds, since for each diamond, we can directly evaluate one term of the sum in (15), with a sign difference, for all four points.

2.3.3 DDFV scheme for the advection-diffusion-reaction equation

Finally, using the discrete operators defined in sections 2.3.1 and 2.3.2, equation (1) can be rewritten in discrete form as follows

$$\begin{array}{rrcl} \forall \mathcal{K} \in \mathcal{P}, & -\mathrm{div}_{\mathcal{K}}^{\mathcal{T}_h} \left(\mu_{\mathcal{K}} \nabla_h q^{\mathcal{T}_h}\right) + \nabla \cdot \left(\mathbf{V} q^{\mathcal{T}_h}\right)_{\mathcal{K}}^{\mathcal{T}_h} + \gamma_{\mathcal{K}} q_{\mathcal{K}}^{\mathcal{T}_h} & = & f_{\mathcal{K}}, \\ \forall \mathcal{K}^* \in \mathcal{P}^*, & -\mathrm{div}_{\mathcal{K}^*}^{\mathcal{T}_h} \left(\mu_{\mathcal{K}^*} \nabla_h q^{\mathcal{T}_h}\right) + \nabla \cdot \left(\mathbf{V} q^{\mathcal{T}_h}\right)_{\mathcal{K}^*}^{\mathcal{T}_h} + \gamma_{\mathcal{K}^*} q_{\mathcal{K}^*}^{\mathcal{T}_h} & = & f_{\mathcal{K}^*}, \end{array} \tag{16}$$

with $\mu_{\mathcal{K}} = \frac{1}{|\mathcal{K}|} \int_{\mathcal{K}} \mu$ and $\mu_{\mathcal{K}^*} = \frac{1}{|\mathcal{K}^*|} \int_{\mathcal{K}^*} \mu$ the finite volume discretization of the term μ in $\mathcal{K}$ or $\mathcal{K}^*$. First, the discrete equations are derived using the second-order accurate approximation (13), leading to

$$\begin{array}{rrcl} \forall \mathcal{K} \in \mathcal{P}, & -\sum_{\nu} \left(\mu_{\mathcal{K}} \nabla_h q_{\mathcal{K}} \cdot \mathbf{N}_\nu + (\mathbf{V}_\nu \cdot \mathbf{N}_\nu) \left[q_{\mathcal{K}} + \nabla_{\mathcal{T}_h} q_{\mathcal{K}} \cdot (x_{\mathcal{K}} - x_\nu) \right] \right) + \gamma_{\mathcal{K}} |\mathcal{K}| q_{\mathcal{K}} & = & |\mathcal{K}| f_{\mathcal{K}}, \\ \forall \mathcal{K}^* \in \mathcal{P}^*, & -\sum_{\nu^*} \left(\mu_{\mathcal{K}^*} \nabla_h q_{\mathcal{K}^*} \cdot \mathbf{N}_{\nu^*} + (\mathbf{V}_{\nu^*} \cdot \mathbf{N}_{\nu^*}) \left[q_{\mathcal{K}^*} + \nabla_{\mathcal{T}_h} q_{\mathcal{K}^*} \cdot (x_{\mathcal{K}^*} - x_{\nu^*}) \right] \right) + \gamma_{\mathcal{K}^*} |\mathcal{K}^*| q_{\mathcal{K}^*} & = & |\mathcal{K}^*| f_{\mathcal{K}^*}. \end{array}$$

These discrete equations can then be rewritten as a linear system as

$$-\mathrm{S}_h^{\mathrm{diff}} q^{\mathcal{T}_h} + \mathrm{S}_h^{\mathrm{adv}} q^{\mathcal{T}_h} + \mathrm{S}_h^{\mathrm{reac}} q^{\mathcal{T}_h} = \mathrm{M}_h f^{\mathcal{T}_h}, \tag{17}$$

where $\mathrm{S}_h^{\mathrm{i}}$ correspond to the stiffness matrices associated with each operator, M_h to the mass matrix, and $f^{\mathcal{T}_h}$ to the vectorized source term. These three matrices are of the following form

$$\mathrm{S}_h^{\mathrm{diff}} = \begin{bmatrix} \mathrm{P}_{\mathrm{P}}^{\mathrm{diff}} & \mathrm{P}_{\mathrm{D}}^{\mathrm{diff}} \\ \mathrm{D}_{\mathrm{P}}^{\mathrm{diff}} & \mathrm{D}_{\mathrm{D}}^{\mathrm{diff}} \end{bmatrix}, \mathrm{S}_h^{\mathrm{adv}} = V_n \begin{bmatrix} \mathrm{I}_P & \mathrm{P}_{\mathrm{D}}^{\mathrm{adv}} \\ \mathrm{D}_{\mathrm{P}}^{\mathrm{adv}} & \mathrm{I}_D \end{bmatrix}, \mathrm{S}_h^{\mathrm{reac}} = \Gamma \mathrm{M}_h, \tag{18}$$

where V_n corresponds to a diagonal matrix containing the coefficients $\mathbf{V}_\nu \cdot \mathbf{N}_\nu$ for each line and Γ to a diagonal with the $\gamma_{\mathcal{K}}$ coefficients. The terms P and D correspond to the primal or dual operations. To efficiently construct the latter, a loop over the diamonds is performed. Furthermore, we can note that this system is sparse and highly parallelizable. In the case of iDDFV, only S_h^{adv} is modified such that

$$\mathrm{S}_h^{\mathrm{adv}} = V_n \begin{bmatrix} 0 & \mathrm{P}_{\mathrm{D}}^{\mathrm{adv}} \\ \mathrm{D}_{\mathrm{P}}^{\mathrm{adv}} & 0 \end{bmatrix}. \tag{19}$$

The last part that remains here is: *how to handle the different boundary conditions.* First, to account for Dirichlet boundary conditions, we use, as for finite element methods [43, 44], a penalization strategy which leads to the following new system to solve

$$\left(-\mathrm{S}_h^{\mathrm{diff}} + \mathrm{S}_h^{\mathrm{adv}} + \mathrm{S}_h^{\mathrm{reac}} + \epsilon^{-1} \mathrm{D}^{\mathrm{pen}}\right) q^{\mathcal{T}_h} = \mathrm{M}_h f^{\mathcal{T}_h} + \epsilon^{-1} G^{\mathrm{D}}, \tag{20}$$

with ϵ a very low value, typically around 10^{-10}, $\mathrm{D}^{\mathrm{pen}}$ a diagonal matrix with one where Dirichlet boundary conditions must be enforced and G^{D} the vector of boundary values at these points. This allows us to handle them the same way for each operator. The Neumann or Robin boundary conditions are taken into account as follows: for the diffusion operator, they are handled seamlessly using the discrete Green formula (9), while for the advection operator $\mathrm{S}_h^{\mathrm{adv}}$ is modified at the boundary points by approximating their normal derivative.

Proposition 2.1 (Robin boundary condition for $\mathrm{S}_h^{\mathrm{diff}}$)**.** *For the diffusion operator, accounting for the Robin boundary condition leads to*

$$(-\mathrm{S}_h^{\mathrm{diff}} + \mathrm{P}_h^{\mathrm{R}})q^{\mathcal{T}_h} = f^{\mathcal{T}_h} + G^R, \tag{21}$$

where

$$\forall \sigma \in \partial\mathcal{T}_h^{\mathrm{R}},\ \forall i_\sigma,\ \mathrm{P}_h^{\mathrm{R}}[i_\sigma, i_\sigma] = \frac{1}{2}\beta|\sigma|,\ \mathrm{P}_h^{\mathrm{R}}[i_\sigma, i_{\sigma_1^*}] = \frac{1}{4}\beta|\sigma|,\ \mathrm{P}_h^{\mathrm{R}}[i_\sigma, i_{\sigma_2^*}] = \frac{1}{4}\beta|\sigma|, \tag{22}$$

and

$$\forall \sigma \in \partial\mathcal{T}_h^{\mathrm{R}},\ \forall i_\sigma,\ G^{\mathrm{R}}[i_\sigma] = \frac{1}{2}g^{\mathrm{R}}(x_\sigma)|\sigma| + \frac{1}{4}\left(g^{\mathrm{R}}(x_{\sigma_1^*}) + g^{\mathrm{R}}(x_{\sigma_2^*})\right)|\sigma|. \tag{23}$$

Proof. Let us apply the discrete Green formula when only accounting for the diffusion part and assuming $\partial\Omega = \Gamma_{\mathrm{R}}$. Indeed, this leads to

$$\begin{aligned} -\left\langle \mathrm{div}^{\mathcal{T}_h}(\mu\nabla_h q), \psi \right\rangle_{\mathcal{F}(\mathcal{T}_h)\times P^1(\mathcal{T}_h)} &= (\mu\nabla_h q, \nabla_h\psi)_{L^2(\mathcal{T}_h)} - (\mu\partial_n q, \mathrm{Tr}_h\psi)_{L^2(\partial\mathcal{T}_h)} \\ &= (\mu\nabla_h q, \nabla_h\psi)_{L^2(\mathcal{T}_h)} - (g^{\mathrm{R}}, \mathrm{Tr}_h\psi)_{L^2(\partial\mathcal{T}_h)} + (\beta q, \mathrm{Tr}_h\psi)_{L^2(\partial\mathcal{T}_h)} \end{aligned}$$

The result is obtained by identifying the first term as the diffusion operator $\mathrm{S}_h^{\mathrm{diff}}$ and applying the discrete trace operator to the other two terms. □

Proposition 2.2 (Robin boundary condition for $\mathrm{S}_h^{\mathrm{adv}}$)**.** *For the advection operator, the matrix $\mathrm{S}_h^{\mathrm{adv}}$ must be modified by calculating the terms on its i_σ-line $\forall \sigma \in \partial\mathcal{T}_h^{\mathrm{R}}$ with*

$$\mu\nabla_h q^{\mathcal{T}_h} \cdot \mathbf{n}_\sigma + \beta q^{\mathcal{T}_h} = g^{\mathcal{T}_h}(x_\sigma)$$

For example, in the case of a conventional orthogonal quadrangular grid along the boundary, accounting for the Robin boundary condition can be reduced to modifying the matrix $\mathrm{S}_h^{\mathrm{adv}}$ as follows

$$\forall \sigma \in \partial\mathcal{T}_h^{\mathrm{R}},\ \forall i_\sigma,\ \mathrm{S}_h^{\mathrm{adv}}[i_\sigma, i_\sigma] = -\frac{h}{2|\mathcal{D}|}\mu + \beta,\ \mathrm{S}_h^{\mathrm{adv}}[i_\sigma, i_{\mathcal{T}}] = \frac{h}{2|\mathcal{D}|}\mu, \tag{24}$$

where $\mathcal{T}$ is the control cell associated with the interface σ. Furthermore, we also must add the term $G_{\mathrm{R}}[i_\sigma] = g(x_\sigma)$ to the source.

Proof. The proof comes directly from the approximation of the normal gradient as $\nabla_h q^{\mathcal{T}_h} \cdot \mathbf{n}_\sigma$, which leads to only one term on the boundary when a standard orthogonal quadrilateral mesh is used for the boundary. In other cases, we shall compute all the terms and modify the line accordingly. □

It shall be noted that, in both cases, Neumann boundary conditions are treated the same way by setting $\beta = 0$ and replacing G^{R} with G^{N}.

2.3.4 An exponential fitting strategy for the advection-diffusion equation

When numerically solving the advection-diffusion equation, in particular in an unsteady state, one can resort to an exponential fitting strategy [7, 8] that allows, using a change of variable, to study a diffusion equation in place of the advection-diffusion one. This has been widely studied in the case of finite element strategy [7, 8, 9] and, more recently, introduced for finite volume schemes [10]. This is particularly useful since, in this case, the coercivity of the operator only depends on the diffusion coefficient.

Indeed, assuming that $\mathbf{V} = \nabla\phi$, i.e., comes from a potential, and that $\gamma = 0$, for simplicity, we can use the following change of variable

$$q(x, y) = \omega(x, y)\rho(x, y),$$

with $\omega(x, y) = \exp\left(-\frac{\phi}{\mu}\right)$ which leads to the following equation for ρ

$$\begin{aligned} -\nabla\cdot(\mu\omega\nabla\rho) &= f, && \text{in } \Omega, \\ \rho &= \omega^{-1}g^{\mathrm{D}}, && \text{on } \Gamma_{\mathrm{D}}, \\ \omega\mu\partial_n\rho + (\mu\partial_n\omega - \omega(\mathbf{V}\cdot\mathbf{n}))\,\rho &= g^{\mathrm{R}}, && \text{on } \Gamma_{\mathrm{R}}. \end{aligned} \tag{25}$$

The latter equation can be extended to $\gamma \neq 0$ easily since it only adds a reaction term of the form $\gamma\omega$. The main advantage of this new equation is that we only have a diffusive term, which can be easily accounted for with DDFV, and that we have a solution if $(\mu\omega)_* \leq \mu\omega \leq (\mu\omega)^*$ almost everywhere, with $(\mu\omega)_* \in \mathbb{R}_*^+$ and $(\mu\omega)^* \in \mathbb{R}_*^+$. This leads to the following linear system to solve

$$\begin{array}{rcl} \forall \mathcal{K} \in \mathcal{P}, & -\sum_\nu \mu_\mathcal{K}\omega_\mathcal{K}\nabla_h q_\mathcal{K} \cdot \mathbf{N}_\nu + \gamma_\mathcal{K}|\mathcal{K}|q_\mathcal{K} & = & |\mathcal{K}|f_\mathcal{K}, \\ \forall \mathcal{K}^* \in \mathcal{P}^*, & -\sum_{\nu^*} \mu_{\mathcal{K}^*}\omega_{\mathcal{K}^*}\nabla_h q_{\mathcal{K}^*} \cdot \mathbf{N}_{\nu^*} + \gamma_{\mathcal{K}^*}|\mathcal{K}^*|q_{\mathcal{K}^*} & = & |\mathcal{K}^*|f_{\mathcal{K}^*}. \end{array}$$

The main difficulty here is that the associated matrix is generally ill-conditioned [10]. In addition, the term $\omega_\mathcal{K} = \frac{1}{\mathcal{K}}\int_\mathcal{K} \omega(x,y)$ can have large variations over the domain and thus a good numerical quadrature is needed, such as a harmonic mean as in [10]. Furthermore, depending on the form of the equation, we shall adapt the exponential fitting, which can also introduce a reaction term. From hereafter, the scheme derived from this strategy will be called exponential fitted DDFV (expfitDDFV).

2.3.5 Some results for the DDFV scheme

Now that the DDFV scheme has been introduced, we show some useful results, particularly for the following numerical tests.

For the advection-diffusion-reaction equation In this part, we assume that $\mathbb{K} = \mathbb{R}$ and study the advection-diffusion-reaction equation (2) under the assumptions given in section 2.1.

Therefore, the following problem is studied

$$\left\{ \begin{array}{rcll} -\nabla \cdot (\mu \nabla q) + \nabla \cdot (\mathbf{V} q) + \gamma q & = & f, & \text{in } \Omega, \\ q & = & g^\mathrm{D}, & \text{on } \Gamma_\mathrm{D}, \\ \mu \partial_n q - (\mathbf{V} \cdot \mathbf{n}) q & = & g^\mathrm{R}, & \text{on } \Gamma_\mathrm{R}, \end{array} \right. \tag{26}$$

In this case, the DDFV scheme reads as solving the following system

$$\left(-\mathrm{S}_h^\mathrm{diff} + \mathrm{P}_h^\mathrm{R} + \epsilon^{-1}\mathrm{D}^\mathrm{pen} + \mathrm{S}_h^\mathrm{adv} - \mathrm{S}_h^\mathrm{reac}\right) q^{\mathcal{T}_h} = \mathrm{M}_h f^{\mathcal{T}_h}, \tag{27}$$

Proposition 2.3. *Problem (27) is well-posed and has a solution.*

Proof. In this case and with the assumptions of the introduction, proof that the DDFV scheme has a solution and converges has been given in [24], and in [45, 46] using a variational formulation. □

For the Helmholtz equation In this part, we assume that $\mathbf{V} = 0$, $\mu = 1$, and $\gamma = -k^2 \in \mathbb{C}$ to study the Helmholtz equation under the assumptions given in 2.1. Furthermore, mixed Dirichlet and Robin boundary conditions are accounted for. This corresponds to the following equation

$$\begin{array}{rcll} -\nabla \cdot (\nabla q) - k^2 q & = & f, & \text{in } \Omega \\ q & = & g^\mathrm{D}, & \text{on } \Gamma^\mathrm{D} \\ \partial_n q & = & g^\mathrm{N}, & \text{on } \Gamma^\mathrm{N} \\ \partial_n q - ikq & = & g^\mathrm{R}, & \text{on } \Gamma^\mathrm{R} \end{array} \tag{28}$$

with $\partial\Omega = \Gamma^\mathrm{D} \cup \Gamma^\mathrm{R}$ and $\mathrm{mes}(\Gamma^\mathrm{D}) \neq 0$. We also assume that $\Re(k) \neq 0$ and $\Im(k) > 0$. The DDFV discretization leads to

$$\left(-\mathrm{S}_h^\mathrm{diff} + \mathrm{P}_h^\mathrm{R} + \epsilon^{-1}\mathrm{D}^\mathrm{pen} - \mathrm{S}_h^\mathrm{reac}\right) q^{\mathcal{T}_h} = \mathrm{M}_h f^{\mathcal{T}_h}, \tag{29}$$

using all the notations defined previously. The goal here is to show that the system is well-posed so that our set of equations admits a solution.

Proposition 2.4. *The problem (29) with $g^\mathrm{D} = 0$ and $g^\mathrm{R} = 0$ is well-posed and admits a solution.*

Proof. First, let us remark that the global matrix $-\mathrm{S}_h^\mathrm{diff} + \mathrm{P}_h^\mathrm{R} + \epsilon^{-1}\mathrm{D}^\mathrm{pen} - \mathrm{S}_h^\mathrm{reac}$ is symmetric since it is the sum of symmetric or diagonal matrices. Second, let us prove that the resulting scheme is coercive. Using the discrete Green formula (9) we obtain

$$(\nabla_h q, \nabla_h \psi)_{L^2(\mathcal{T}_h)} - (ikq, \psi)_{L^2(\partial\mathcal{T}_h)} - (k^2 q, \psi)_{L^2(\mathcal{T}_h)} = (f, \psi)_{L^2(\mathcal{T}_h)}.$$

We denote by $a(q,\psi)$ the bilinear form on the left side and by $b(\psi)$ the continuous linear form on the right side. The goal is thus to show that $a(q,\psi)$ is coercive. To do so, we set $\Psi = -ikq$. Indeed, this leads to

$$a(q,-ikq) = (i\bar{k}\nabla_h q, \nabla_h q)_{L^2(\mathcal{T}_h)} + (|k|^2 q, q)_{L^2(\partial\mathcal{T}_h)} - (ik|k|^2 q, q)_{L^2(\mathcal{T}_h)}$$

Finally, using $i\bar{k} = \Im(k) - i\Re(k)$ and $ik = -\Im(k) + i\Re(k)$ and taking the real part we get

$$\begin{aligned}\Re(a(q,-ikq)) &= (\Im(k)\nabla_h q, \nabla_h q)_{L^2(\mathcal{T}_h)} + (|k|^2 q, q)_{L^2(\partial\mathcal{T}_h)} + (\Im(k)|k|^2 q, q)_{L^2(\mathcal{T}_h)} \\ &\geq \left(\Im(k)\min(1,|k|^2) + C^2|k|^2\right)\|u\|_{L^2(\mathcal{T}_h)}\end{aligned}$$

We can conclude that a is coercive since $|k||a(q,q)| = |a(q,-ikq)| \geq \Re(a(q,-ikq))$. Therefore, this concludes the proof since the system matrix is symmetric and a is coercive [16]. For more general results on the coercivity of the sequilinear form $a(\cdot,\cdot)$, we refer the readers to [47, 48, 49], where the proof is performed in general using Gårding's lemma or Fredholm's alternative. □

Furthermore, if non-homogeneous boundary conditions are accounted for, we can derive the same results by changing variables.

3 Numerical tests

This section is devoted to numerical tests that validate the DDFV scheme to solve problems (26) and (28). Furthermore, we also compare the different strategies introduced to solve the advection-diffusion-reaction equation (26) in terms of accuracy. To validate their expected behaviors, we study the following three approximation errors

$$\begin{aligned}E_{\max}(q^{\mathcal{T}_h}) &= \frac{\max_{x\in\mathcal{T}_h}(|q_{\text{ex}}(x) - q^{\mathcal{T}_h}(x)|)}{\max_{x\in\mathcal{T}_h}(|q_{\text{ex}}(x)|)}, \\ E_1(q^{\mathcal{T}_h}) &= \frac{\|q_{\text{ex}} - q^{\mathcal{T}_h}\|_1}{\|q_{\text{ex}}\|_1}, \\ E_2(q^{\mathcal{T}_h}) &= \frac{\|q_{\text{ex}} - q^{\mathcal{T}_h}\|_2}{\|q_{\text{ex}}\|_2}.\end{aligned} \tag{30}$$

In each case, we will study the convergence with the mesh size $h = \min(h_y, h_y)$ over a conventional $N_x \times N_y$ Cartesian quadrangular mesh, and a randomly distorted one [50]. The latter is constructed as follows. From a conventional Cartesian mesh, we randomly move each point inside the domain according to

$$\begin{aligned}\forall (i,j) \in [1,N_x]\times[1,N_y],\ x_{ij} &= x_{ij} + \sigma h_x(R_x - 0.5) \\ y_{ij} &= y_{ij} + \sigma h_y(R_y - 0.5),\end{aligned} \tag{31}$$

where σ is the distortion factor. We will use $\sigma = 0.5$ in all the numerical examples corresponding to a highly distorted mesh. In Figures 4 (a) and (b), we give an example of a Cartesian mesh with its distorted counterpart, respectively.

In the case of the advection-diffusion-reaction equation, the three schemes DDFV, iDDFV, and the exponential fitted DDFV (denoted as expfitDDFV) will also be compared in terms of conditioning.

In addition, the Python codes used for all the tests are available at the following link: https://github.com/thobonensta/mDDFV. We are currently developing a Fortran-based version of the code using the Hypre LLNL library [51].

3.1 Solving equation (26) with DDFV

3.1.1 Homogeneous Dirichlet boundary conditions

In this case, we solve (26) in the computational domain $\Omega = [0,1]\times[0,1]$. We set $\mu = 1$, $\mathbf{V} = [2,1]$ and $\gamma = 1$. Furthermore, the source term and the boundary conditions are computed so that

$$q_{\text{ex}}(x,y) = x(x-1)y(y-1), \tag{32}$$

is the exact solution of (26). On the boundary, we have $\Gamma_{\text{R}} = \emptyset$ and $\Gamma_{\text{D}} = \partial\Omega$ such that $g^{\text{D}} = 0$. The parameters are chosen so that the diffusion and advection coefficients are of the same order.

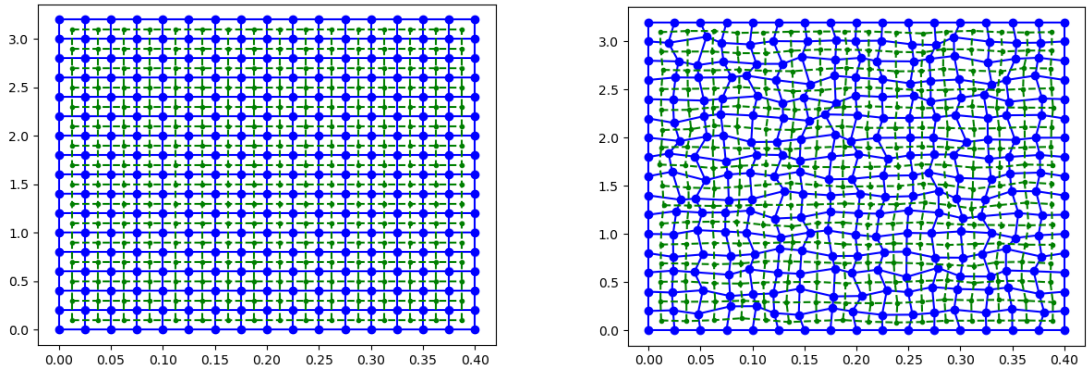

(a) Cartesian grid 16×16 (b) Distorted mesh

Figure 4: Example of a Cartesian quadrangular grid and its distorted counterpart.

In Figures 5 (a) and (b), we plot $q^{\mathcal{T}_h}$ and $q_{\text{ex}}(x_{\mathcal{T}_h})$ for a Cartesian grid with 128×128 points, respectively. Then, in Figure 6, we plot the error convergence for E_2 with h on the conventional and distorted meshes for DDFV, iDDFV, and expfitDDFV. In the legend, α denotes the computed rate of convergence. We also report all the different errors for the different meshes in Table 1 when the standard DDFV scheme is applied, in Table 2 for iDDFV, and Table 3 when the exponential fitting technique is applied. Finally, in Table 4, we report the different condition numbers for different step sizes for the three methods.

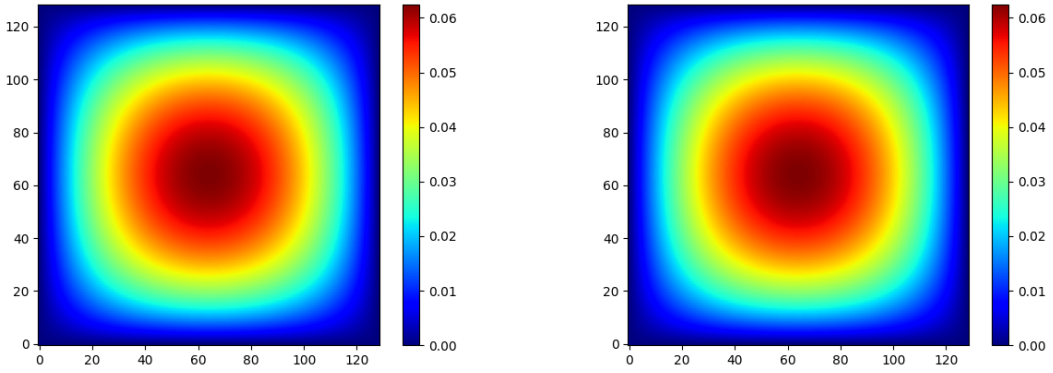

(a) $q^{\mathcal{T}_h}$ computed with DDFV. (b) Projection of the exact solution q_{ex} in $\mathcal{T}_h$

Figure 5: Evolution of $q^{\mathcal{T}_h}$ and q_{ex} over the domain Ω when a 128×128 cells mesh is considered in the case of homogeneous Dirichlet boundary conditions.

This test shows that the three methods are working well. Indeed, we obtain the same accuracy with DDFV, iDDFV, and expfitDDFV as expected. Furthermore, the convergence is of order 2 for all the methods, corresponding to the super-convergence order usually exhibited by DDFV [16]. It shall be noted that the exponential fitted strategy is computationally less intensive and easier to implement at the cost of a highly ill-conditioned matrix, see Table 4, compared to DDFV and iDDFV.

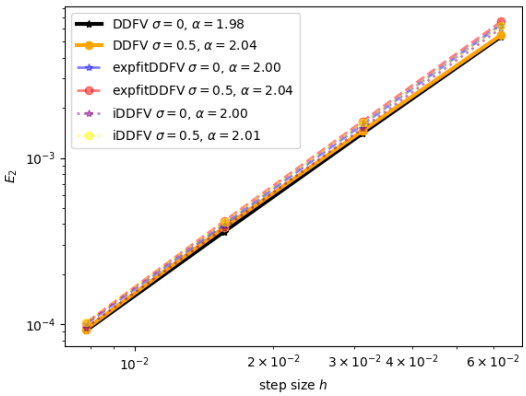

Figure 6: Evolution of the l^2 error with respect to h in a LogLog scale. The star and dot marker correspond to the conventional and distorted mesh, while the plain, dotted, and dashed lines correspond to the standard, iDDFV, and expfitDDFV, respectively.

	Cartesian grid			Distorted grid		
$N_x \times N_y$	E_1	E_2	E_∞	E_1	E_2	E_∞
16×16	4.7×10^{-3}	5.4×10^{-3}	3.7×10^{-3}	5.3×10^{-3}	5.5×10^{-3}	5.7×10^{-3}
32×32	1.5×10^{-3}	1.4×10^{-3}	1.0×10^{-3}	1.5×10^{-3}	1.5×10^{-3}	1.7×10^{-3}
64×64	3.2×10^{-4}	3.6×10^{-4}	2.4×10^{-4}	3.6×10^{-4}	3.8×10^{-4}	4.4×10^{-4}
128×128	8.1×10^{-5}	9.1×10^{-5}	6.1×10^{-5}	8.9×10^{-5}	9.3×10^{-5}	1.3×10^{-4}

Table 1: Evolution of E_1, E_2, and E_∞ over the number of unknowns when considering a Cartesian or distorted grid when homogeneous Dirichlet boundary conditions are considered for the DDFV scheme.

	Cartesian grid			Distorted grid		
$N_x \times N_y$	E_1	E_2	E_∞	E_1	E_2	E_∞
16×16	5.5×10^{-3}	6.1×10^{-3}	4.0×10^{-3}	6.2×10^{-3}	6.2×10^{-3}	7.2×10^{-3}
32×32	1.4×10^{-3}	1.5×10^{-3}	1.0×10^{-3}	1.7×10^{-3}	1.6×10^{-3}	2.0×10^{-3}
64×64	3.4×10^{-4}	3.8×10^{-4}	2.5×10^{-4}	3.9×10^{-4}	4.1×10^{-4}	5.3×10^{-4}
128×128	8.5×10^{-5}	9.5×10^{-5}	6.3×10^{-5}	9.7×10^{-5}	1.0×10^{-4}	1.3×10^{-4}

Table 2: Evolution of E_1, E_2, and E_∞ over the number of unknowns when considering a Cartesian or distorted grid when homogeneous Dirichlet boundary conditions are considered for the iDDFV scheme.

	Cartesian grid			Distorted grid		
$N_x \times N_y$	E_1	E_2	E_∞	E_1	E_2	E_∞
16×16	5.6×10^{-3}	6.3×10^{-3}	7.3×10^{-3}	6.0×10^{-3}	6.6×10^{-3}	9.9×10^{-3}
32×32	1.4×10^{-3}	1.6×10^{-3}	1.9×10^{-3}	1.6×10^{-3}	1.7×10^{-3}	1.9×10^{-3}
64×64	3.6×10^{-4}	4.0×10^{-4}	4.8×10^{-4}	3.9×10^{-4}	4.1×10^{-4}	7.0×10^{-4}
128×128	9.1×10^{-5}	1.0×10^{-4}	1.2×10^{-4}	1.0×10^{-4}	1.0×10^{-4}	1.8×10^{-4}

Table 3: Evolution of E_1, E_2, and E_∞ over the number of unknowns when considering a Cartesian or distorted grid when homogeneous Dirichlet boundary conditions are considered for the expfitDDFV scheme.

	DDFV	iDDFV	expfitDDFV
16×16	3.4×10^3	3.3×10^3	32.8×10^3
32×32	12.3×10^3	11.9×10^3	106.1×10^3
64×64	45.5×10^3	45.2×10^3	381.1×10^3

Table 4: Evolution of the condition number of the matrix associated with each method with the grid size.

3.1.2 Non-homogeneous Dirichlet boundary conditions

In this case, we solve (26) in the computational domain $\Omega = [0,1]\times[0,1]$. Here, we set $\mu = 5$, $\mathbf{V} = [1,1]$ and $\gamma = 1$. Furthermore, the source term and the boundary conditions are computed so that

$$q_{\text{ex}}(x,y) = x\cos(x) + y\sin(y) + 1 \tag{33}$$

is the exact solution of (26).

First, let us study the case where only Dirichlet boundary conditions are accounted for, so that $\partial\Omega = \Gamma_{\text{D}}$ and $\Gamma_{\text{R}} = \emptyset$, and g^{D} calculated so that q_{ex} is the exact solution.

In Figures 7 (a) and (b), we plot $q^{\mathcal{T}_h}$ and $q_{\text{ex}}(x_{\mathcal{T}_h})$ for a Cartesian grid with 128×128 points, respectively. Then, in Figure 8, we plot the error convergence for E_2 with h on the conventional and distorted meshes. In the legend, α denotes the computed rate of convergence. We also report all the different errors for the different meshes in Table 5 when the standard DDFV scheme is applied, in Table 7 for iDDFV, and in Table 6 when the exponential fitting technique is applied.

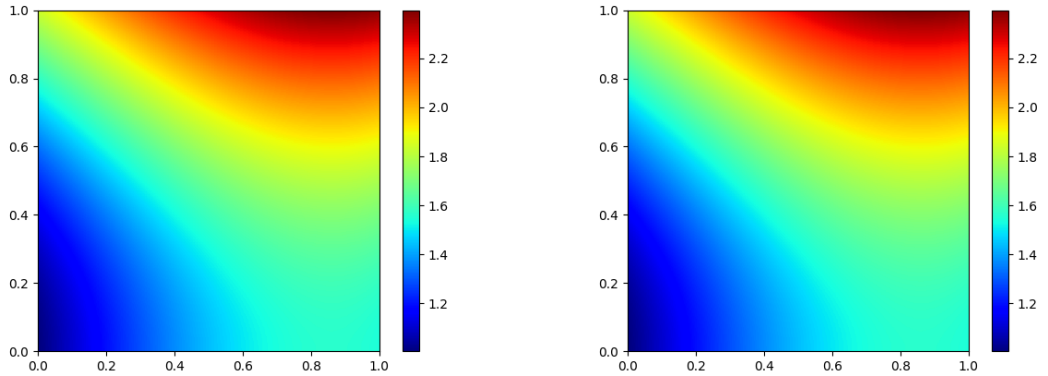

(a) $q^{\mathcal{T}_h}$ computed with DDFV.

(b) Projection of the exact solution q_{ex} in $\mathcal{T}_h$

Figure 7: Evolution of $q^{\mathcal{T}_h}$ and q_{ex} over the domain Ω when a 128×128 cells mesh is considered.

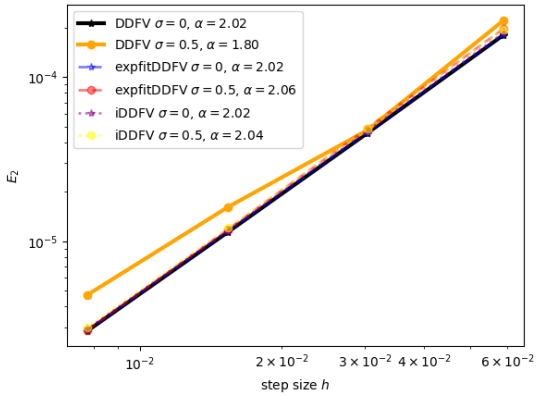

Figure 8: Evolution of the l^2 error with respect to h in a LogLog scale. The star and dot marker correspond to the conventional and distorted mesh, while the plain and dashed lines correspond to the standard and exponential fit DDFV, respectively.

In this case, the proposed methods (DDFV and iDDFV) work well. Indeed, the error is low, and we observe a second-order convergence, even when a highly distorted mesh is considered. In addition, errors are of the same level for the conventional and distorted mesh, showing that the methods are quite

	Cartesian grid			Distorted grid		
$N_x \times N_y$	E_1	E_2	E_∞	E_1	E_2	E_∞
16×16	3.4×10^{-4}	1.8×10^{-4}	4.1×10^{-4}	3.3×10^{-4}	2.2×10^{-4}	6.7×10^{-4}
32×32	9.6×10^{-5}	4.5×10^{-5}	1.1×10^{-4}	1.3×10^{-4}	4.7×10^{-5}	3.2×10^{-4}
64×64	2.5×10^{-5}	1.1×10^{-5}	2.8×10^{-5}	6.0×10^{-5}	1.6×10^{-5}	2.1×10^{-4}
128×128	6.6×10^{-6}	2.9×10^{-6}	7×10^{-6}	3.1×10^{-5}	4.7×10^{-6}	9.9×10^{-5}

Table 5: Evolution of E_1, E_2, and E_∞ over the number of unknowns when considering a Cartesian or distorted grid when Dirichlet boundary conditions are considered for the DDFV scheme.

	Cartesian grid			Distorted grid		
$N_x \times N_y$	E_1	E_2	E_∞	E_1	E_2	E_∞
16×16	3.4×10^{-4}	1.8×10^{-4}	4.1×10^{-4}	4.0×10^{-4}	2.0×10^{-4}	5.8×10^{-4}
32×32	9.6×10^{-5}	4.6×10^{-5}	1.1×10^{-4}	9.9×10^{-5}	4.9×10^{-5}	1.5×10^{-4}
64×64	2.6×10^{-5}	1.2×10^{-5}	2.7×10^{-5}	2.7×10^{-5}	1.2×10^{-5}	4.7×10^{-5}
128×128	6.6×10^{-6}	2.9×10^{-6}	6.8×10^{-6}	6.9×10^{-6}	2.9×10^{-6}	1.2×10^{-5}

Table 6: Evolution of E_1, E_2, and E_∞ over the number of unknowns when considering a Cartesian or distorted grid when Dirichlet boundary conditions are considered, when the exponential fitting is applied.

	Cartesian grid			Distorted grid		
$N_x \times N_y$	E_1	E_2	E_∞	E_1	E_2	E_∞
16×16	3.5×10^{-4}	1.9×10^{-4}	5.6×10^{-4}	3.4×10^{-4}	1.8×10^{-4}	4.1×10^{-4}
32×32	9.7×10^{-5}	4.9×10^{-5}	1.6×10^{-4}	9.6×10^{-5}	4.7×10^{-5}	1.1×10^{-4}
64×64	2.5×10^{-5}	1.2×10^{-5}	4.9×10^{-5}	2.5×10^{-5}	1.2×10^{-5}	2.8×10^{-5}
128×128	6.6×10^{-6}	3.0×10^{-6}	1.3×10^{-5}	6.6×10^{-6}	2.9×10^{-6}	7.0×10^{-6}

Table 7: Evolution of E_1, E_2, and E_∞ over the number of unknowns when considering a Cartesian or distorted grid when Dirichlet boundary conditions are considered for the iDDFV scheme.

stable to the mesh configuration. Furthermore, the convergence result was expected in this case, since in general DDFV exhibits a super convergence of order 2 [16], even if error estimates show an $O(h)$ order [24]. In addition, we obtain similar results with the exponential fitting procedure, as expected. Nonetheless, the latter allows us to avoid implementing the advection operator matrix, leading to a better computation time and space complexity. We can also remark that the exponential fitting DDFV scheme is slightly more stable with the distorted mesh. Nonetheless, as a reminder from the previous test, the matrix associated with expfit DDFV is ill-conditioned compared to the other two.

To conclude this test, we conduct a numerical experiment on the robustness of the method with the advection coefficient. Indeed, one of the main difficulty is the convection dominated case. To do so, we set the diffusion and reaction coefficients to $\mu = \gamma = 1$, we use the 32×32 mesh. Furthermore, as before, we consider either a conventional Cartesian mesh or its distorted version. Therefore, for different particle velocities we report the results in terms of the different errors in Table 8. To make it more readable and easily compare the three methods, we obly report the E_2 error.

	Cartesian grid			Distorted grid		
$\mathbf{V}$	DDFV	iDDFV	expfitDDFV	DDFV	iDDFV	expfitDDFV
$[1, 1]$	1.9×10^{-4}	4.6×10^{-5}	5.7×10^{-5}	1.7×10^{-4}	4.8×10^{-5}	5.8×10^{-5}
$[10, 10]$	1.2×10^{-2}	4.5×10^{-5}	1.1×10^{-3}	1.7×10^{-2}	4.7×10^{-5}	1.1×10^{-3}
$[100, 100]$	8.3×10^{-2}	$1.2 \times 6.0 \times 10^{-5}$	-	-	6.8×10^{-5}	-
$[1000, 1000]$	-	4.8×10^{-4}	-	-	5.0×10^{-4}	-

Table 8: Evolution of E_2 with $\mathbf{V}$ when considering a Cartesian or distorted grid and the three different methods. The '-' means the method failed to give an accurate result.

From this table we can conclude that the iDDFV scheme is robust to the advection coefficient, while the other struggle with convection dominant case. For the expfitDDFV, we think that it is mostly due to the exponential change of variable boundary conditions. In addition, the error of DDFV is in line, with the one obtained in [24]. The advantage of the interpolation, i.e., iDDFV, might comes from the fact that we approximate to high order the quantity of interest on the interface directly.

In conclusion, we recommend to use the iDDFV strategy over DDFV or the expfitDDFV since it can be used in any setup.

3.1.3 The mixed boundaries case

Thirdly, let us study the case where mixed boundary conditions are accounted for. The parameters and the exact solution remain the same as in the previous test. Nonetheless, here, we consider Robin boundary condition, i.e. Γ^{R}, on the left of the domain and Dirichlet boundary conditions, i.e. Γ^{D}, on the rest of the border. As before, we analyze the behavior of DDFV for the three errors defined in (30). For h decreasing, we report the different errors in the Cartesian or distorted grid case in Table 9 for the standard DDFV scheme, in Table 11 for iDDFV, and in Table 10 for its exponential fitted counterpart. In Figure 9, we also plot the convergence of $E_2(h)$.

	Cartesian grid			Distorted grid		
$N_x \times N_y$	E_1	E_2	E_∞	E_1	E_2	E_∞
16×16	6.5×10^{-4}	8.6×10^{-4}	1.9×10^{-3}	6.6×10^{-4}	8.6×10^{-4}	1.9×10^{-3}
32×32	2.6×10^{-4}	3.4×10^{-4}	7.8×10^{-4}	2.5×10^{-4}	3.3×10^{-4}	7.5×10^{-4}
64×64	1.1×10^{-4}	1.5×10^{-4}	3.5×10^{-4}	1.2×10^{-4}	1.5×10^{-4}	3.5×10^{-4}
128×128	5.4×10^{-5}	7.2×10^{-5}	1.6×10^{-4}	5.3×10^{-5}	7.1×10^{-5}	1.6×10^{-4}

Table 9: Evolution of E_1, E_2, and E_∞ over the number of unknowns when considering a Cartesian or distorted grid in the case of mixed boundary conditions for the standard DDFV scheme.

Here, we observe a convergence of order 1 numerically, which corresponds to the error estimate of DDFV [2, 3, 24]. This could be due to the approximation of the integral on the boundary for the Robin boundary condition. Nonetheless, as before, we can see that the methods work well even when a highly distorted mesh is considered. Furthermore, here we can see that the exponential fitted strategy is better in terms of accuracy, which is normal since we approximate the Robin boundary condition

	Cartesian grid			Distorted grid		
$N_x \times N_y$	E_1	E_2	E_∞	E_1	E_2	E_∞
16×16	4×10^{-4}	4.5×10^{-4}	7.5×10^{-4}	4.5×10^{-4}	4.5×10^{-4}	8.1×10^{-4}
32×32	1.3×10^{-4}	1.8×10^{-4}	3.3×10^{-4}	1.4×10^{-4}	1.7×10^{-4}	3.6×10^{-4}
64×64	5.6×10^{-5}	7.3×10^{-5}	1.6×10^{-4}	5.8×10^{-5}	7.3×10^{-5}	1.6×10^{-4}
128×128	2.6×10^{-5}	3.4×10^{-5}	7.6×10^{-5}	2.6×10^{-5}	3.5×10^{-5}	7.9×10^{-5}

Table 10: Evolution of E_1, E_2, and E_∞ over the number of unknowns when considering a Cartesian or distorted grid in the case of mixed boundary conditions for the expfitDDFV scheme.

	Cartesian grid			Distorted grid		
$N_x \times N_y$	E_1	E_2	E_∞	E_1	E_2	E_∞
16×16	6.4×10^{-4}	8.3×10^{-4}	1.8×10^{-3}	6.6×10^{-4}	8.7×10^{-4}	1.9×10^{-3}
32×32	2.6×10^{-4}	3.4×10^{-4}	7.8×10^{-4}	2.6×10^{-4}	3.5×10^{-4}	7.9×10^{-4}
64×64	1.2×10^{-4}	1.6×10^{-4}	3.6×10^{-4}	1.2×10^{-4}	1.6×10^{-4}	3.5×10^{-4}
128×128	5.4×10^{-5}	7.2×10^{-5}	1.6×10^{-4}	5.6×10^{-5}	7.4×10^{-5}	1.6×10^{-4}

Table 11: Evolution of E_1, E_2, and E_∞ over the number of unknowns when considering a Cartesian or distorted grid in the case of mixed boundary conditions for the iDDFV scheme.

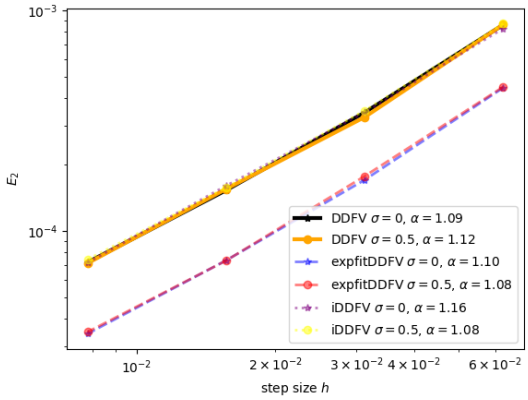

Figure 9: Plot of $E_2(h)$ in a LogLog scale for the mixed boundary conditions case. The same legend as in Figure 8 is used here.

once here, for the diffusion operator, while we need to approximate it twice for the DDFV schemes, i.e., for the diffusion and the advection operators.

In conclusion, these tests have shown that the DDFV scheme works well for the advection-diffusion-reaction equation with mixed boundary conditions (26).

3.2 Solving Helmholtz equation (28) with DDFV

Here, we study the Helmholtz equation (28). For all the tests, we set $k = 2\pi/\lambda$, with $\lambda = c/f$ and $f = 300$ MHz. As before, the numerical experiments are here to validate the behavior of DDFV in this case.

3.2.1 The Dirichlet boundary case

Here, we consider solely Dirichlet boundaries so that $\partial\Omega = \Gamma^{\mathrm{D}}$. Furthermore, equation (28) is solved in the domain $\Omega = [0, 0.4] \times [0, 3.2]$, and the source term as well as the boundary term are calculated so that

$$q_{\mathrm{ex}}(x, y) = \sin\left(2\pi \frac{x}{x_{\max}}\right) \sin\left(2\pi \frac{y}{y_{\max}}\right)$$

is the exact solution. This corresponds to accounting for a homogeneous Dirichlet boundary condition. First, in Figure 10 (a), we plot $q^{\mathcal{T}_h}$ obtained with DDFV when a mesh with 128×128 elements is considered. In Figure 10 (b), the absolute difference with q_{ex} is provided in this case.

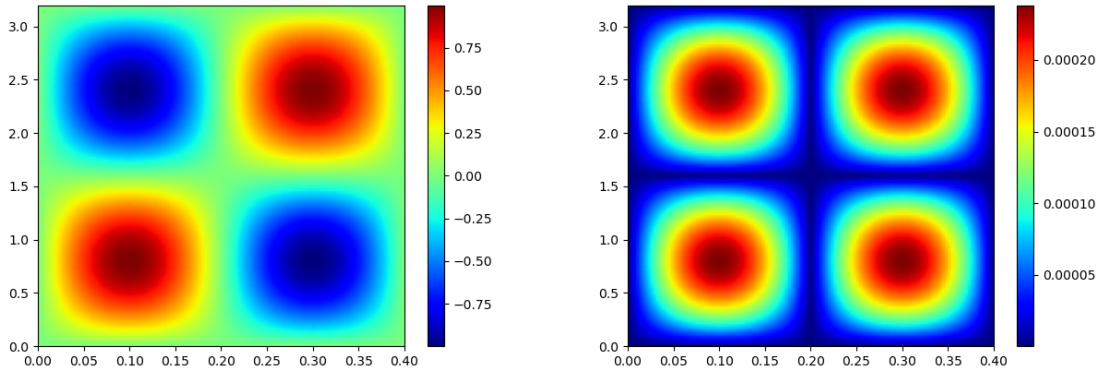

(a) $q^{\mathcal{T}_h}$ in Ω computed with DDFV.

(b) Absolute difference $|q_{\mathrm{ex}}(\mathcal{T}_h) - q^{\mathcal{T}_h}|$

Figure 10: Plot of the electric field computed in Ω with DDFV and of the absolute difference with the exact solution. Here a 128×128 control volumes mesh is used.

Here, we can see that the overall variations as well as the Dirichlet boundary conditions are well taken into account. Furthermore, the error absolute difference is relatively low.

Second, to better observe the behavior of DDFV in this case, we plot the convergence of E_2 with h in Figure 11. In this case, the two lines correspond to the conventional or distorted mesh, while α in the legend is the numerical convergence rate.

We also report in Table 12 the variation of the three measured errors with increasing control volumes when either the Cartesian mesh or its distorted counterpart is considered.

From Figure 11 and Table 12, we observe a convergence of order 2, as expected from the literature and the previous tests. In addition, even on the distorted mesh, the error is of the same order as on the conventional mesh, showing the robustness of the method to the mesh. This test thus shows that the method works well to solve the Helmholtz equation with Dirichlet boundary conditions.

3.2.2 Accounting for an absorbing boundary condition

Now, we consider the case of mixed boundary conditions. To be more precise, in this case, one can consider q as the total field, i.e., the sum of the incident and scattered fields. Moreover, we consider

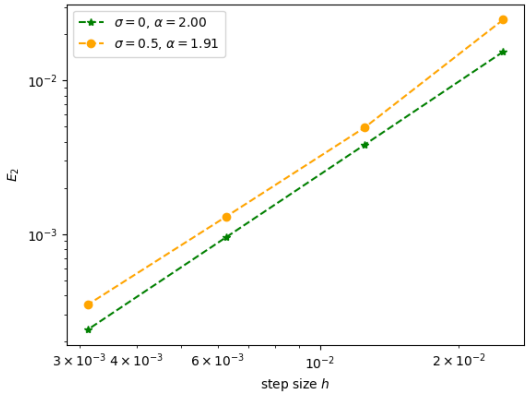

Figure 11: Plot of $E_2(h)$ in a LogLog scale. The star and dot marker correspond to the conventional and distorted mesh.

	Cartesian grid			Distorted grid		
$N_x \times N_y$	E_1	E_2	E_∞	E_1	E_2	E_∞
16×16	1.5×10^{-2}	1.5×10^{-2}	1.5×10^{-2}	3.8×10^{-2}	2.5×10^{-2}	5.5×10^{-2}
32×32	3.8×10^{-3}	3.8×10^{-3}	3.8×10^{-3}	7.4×10^{-3}	4.9×10^{-3}	1.2×10^{-2}
64×64	9.5×10^{-4}	9.5×10^{-4}	9.5×10^{-4}	2.3×10^{-3}	1.3×10^{-3}	3.6×10^{-3}
128×128	2.4×10^{-4}	2.4×10^{-4}	2.4×10^{-4}	5.8×10^{-4}	3.5×10^{-4}	1.3×10^{-3}

Table 12: Evolution of E_1, E_2, and E_∞ over the number of unknowns when considering a Cartesian or distorted grid in the case of Dirichlet boundaries.

the incident field to be a plane wave of amplitude 1 coming from an angle θ_i. This leads to the interior problem, and the Robin boundary condition allows us to approximate the Sommerfeld condition and to account easily for the incident plane wave. Thus, this problem is widely studied in the literature [6] since it is useful for many applications.

In particular, here we consider a plane wave coming from $\theta_i = 0°$. The computation domain is $\Omega = [0, 1] \times [0, 1]$. Furthermore, an absorbing boundary condition is accounted for on the right side of the domain with

$$g^{\mathrm{R}}(1, y) = i(k - \mathbf{k}_i \cdot \mathbf{n}) \exp\left(-i\mathbf{k}_i \cdot \mathbf{x}\right),$$

where $\mathbf{n}$ is the exterior normal, $\mathbf{k}_i = [-k\cos(\theta_i), -k\sin(\theta_i)]$ the incident wave vector, and $\mathbf{x}$ the position in Ω. The upper and lower boundaries are considered to be homogeneous Neumann conditions, while the left one is a homogeneous Dirichlet condition, which models a perfect electric conductor. In this case, the exact solution is the sum of the incident plane wave and its reflection.

The absolute value of the solution $q^{\mathcal{T}_h}$ computed with DDFV is plotted in Figure 12 (a). Indeed, here we obtain a solution $q \in \mathbb{C}$. In addition, as for the previous test case, we plot the absolute difference with the exact solution in Figure 12 (b).

As before, one can see that DDFV works well in this case. Indeed, we can see that the total field computed respects the behavior of the exact solution, with sinusoidal variations, as expected. Furthermore, the absolute difference is low, and the error is mainly distributed on the absorbing boundary condition.

To better observe the behavior of DDFV, we plot the evolution of E_2 with h in Figure 13. In the latter, the star and circle marker correspond to a Cartesian mesh or its distorted counterpart. In addition, we report in Table 13 the different errors (30) for the different studied cases.

As for the previous test case, i.e., with only Dirichlet conditions, we observe second-order convergence, even on the distorted mesh. Furthermore, the errors in the conventional and distorted mesh are quite close, again showing the method's robustness with the mesh distribution. We can thus conclude that DDFV performs well in this case, and can hence be used to solve the Helmholtz equation and to study electromagnetic problems.

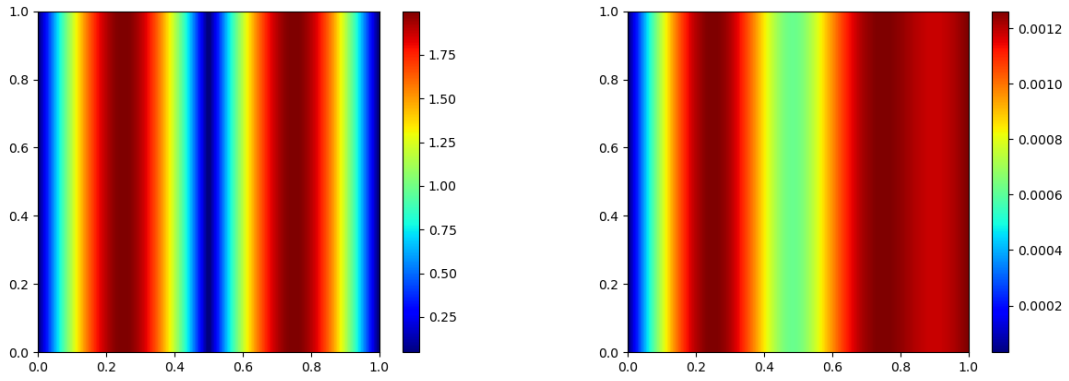

(a) $|q^{\mathcal{T}_h}|$ in Ω computed with DDFV.

(b) Absolute difference with the exact solution

Figure 12: Electric field computed with DDFV, i.e. $q^{\mathcal{T}_h}$ and absolute difference with the exact solution. As before, a 128×128 control volume mesh is used for this plot.

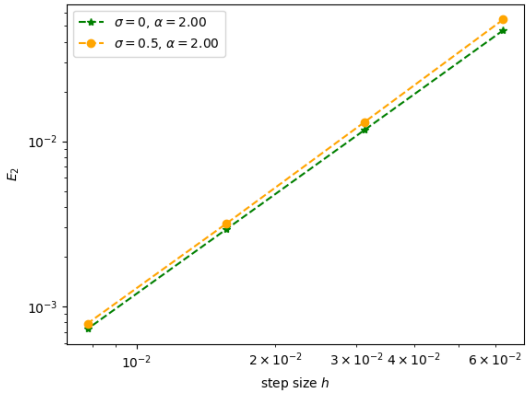

Figure 13: Plot of $E_2(h)$ in a LogLog scale for the mixed boundary conditions case. The same legend as in Figure 11 is used here.

	Cartesian grid			Distorted grid		
$N_x \times N_y$	E_1	E_2	E_∞	E_1	E_2	E_∞
16×16	5.0×10^{-2}	4.7×10^{-2}	4.1×10^{-2}	5.9×10^{-2}	5.4×10^{-2}	5.3×10^{-2}
32×32	1.2×10^{-2}	1.2×10^{-2}	1.0×10^{-2}	1.4×10^{-2}	1.3×10^{-2}	1.3×10^{-2}
64×64	3.1×10^{-3}	2.9×10^{-3}	2.5×10^{-3}	3.5×10^{-3}	3.2×10^{-3}	4.1×10^{-3}
128×128	7.8×10^{-4}	7.3×10^{-4}	6.3×10^{-4}	8.8×10^{-4}	7.9×10^{-4}	1.1×10^{-3}

Table 13: Evolution of E_1, E_2, and E_∞ over the number of unknowns when considering a Cartesian or distorted grid in the case of mixed boundary conditions.

4 Conclusion

In this paper, we proposed a self-consistent DDFV method to solve the steady-state advection-diffusion-reaction equation with mixed boundary conditions. In particular, we proposed two different strategies to handle the advection term in DDFV. We also presented and compared our approach to an exponential-fitted DDFV scheme.

We first extended the approach of [24] by incorporating a reaction term and handling mixed boundary conditions, and also proposed another way to handle the advection term using the primal/dual mesh. A key novelty of our work is that we did not restrict ourselves to real-valued solutions, allowing us to address the Helmholtz equation as well. This led to a discrete formulation of the advection-diffusion-reaction equation on the primal/dual mesh of DDFV. We established the existence of a solution in two relevant cases. We have also shown that the traditional tools of finite elements can be used with DDFV, facilitating the implementation of absorbing and Neumann boundary conditions. Moreover, unlike traditional finite volume methods, DDFV imposes no constraints on the mesh structure, making it particularly suited for complex geometries.

To validate the method, we performed an in-depth numerical analysis on two important problems: the advection-diffusion-reaction equation with mixed boundary conditions, relevant in plasma modeling, and the Helmholtz equation with absorbing boundary conditions, used to describe scattered fields. The results confirmed that the method generally achieves second-order superconvergence and remains stable even on highly distorted meshes. For the advection-diffusion-reaction equation, the observed $O(h)$ error is consistent with theoretical predictions [24] and could also be explained by the approximation of the boundary integrals. In addition, we tested the robustness of the proposed approaches for different advection coefficient and have shown that it seems best to use the proposed iDDFV scheme in general since it performs well even in convection dominated regime.

This generalization of DDFV significantly broadens its potential applications in electromagnetic. It provides an alternative to the finite element method for modeling scattered fields, particularly in cases involving thin layers, where finite volume schemes offer a natural way to handle jump conditions [2, 5]. Additionally, we are currently exploring its use in tunnel propagation problems, where the parabolic wave equation is traditionally solved using finite differences [52, 53]. The flexibility of DDFV makes it particularly well-suited for handling complex structures in such scenarios.

Moving forward, our main focus is to extend the method to unsteady problems, particularly for solving the drift-diffusion model [11] used in cold plasma modeling.

Acknowledgment

The authors would like to thank the "GDR Emili" for their support in the collaboration between the authors.

References

[1] F. Hermeline, "A finite volume method for the approximation of diffusion operators on distorted meshes," *Journal of Computational Physics*, vol. 160, no. 2, pp. 481–499, 2000.

[2] F. Boyer and F. Hubert, "Finite volume method for 2D linear and nonlinear elliptic problems with discontinuities," *SIAM Journal on Numerical Analysis*, vol. 46, no. 6, pp. 3032–3070, 2008.

[3] Y. Coudière, C. Pierre, and R. Turpault, "A 2d/3d finite volume method used to solve the bidomain equations of electrocardiology," in *Algoritmy 2009*, pp. 1–10, 2009.

[4] S. Krell and J. Moatti, "Structure-preserving schemes for drift-diffusion systems on general meshes: DDFV versus HFV," in *International Conference on Finite Volumes for Complex Applications*, pp. 325–334, Springer, 2023.

[5] T. Bonnafont, D. Bessières, and J. Paillol, "A finite volume method to solve the Poisson equation with jump conditions and surface charges: Application to electroporation," *Journal of Computational Physics*, vol. 504, p. 112862, 2024.

[6] E. Heikkola, T. Rossi, and J. Toivanen, "Fast direct solution of the Helmholtz equation with a perfectly matched layer or an absorbing boundary condition," *International Journal for Numerical Methods in Engineering*, vol. 57, no. 14, pp. 2007–2025, 2003.

[7] F. Brezzi, L. D. Marini, and P. Pietra, "Two-dimensional exponential fitting and applications to drift-diffusion models," *SIAM Journal on Numerical Analysis*, vol. 26, no. 6, pp. 1342–1355, 1989.

[8] J. I. Ramos, "On diffusive methods and exponentially fitted techniques," *Applied Mathematics and Computation*, vol. 103, no. 1, pp. 69–96, 1999.

[9] Y. Shih, J.-Y. Cheng, and K.-T. Chen, "An exponential-fitting finite element method for convection–diffusion problems," *Applied mathematics and computation*, vol. 217, no. 12, pp. 5798–5809, 2011.

[10] C. Chainais-Hillairet, M. Herda, S. Lemaire, and J. Moatti, "Long-time behaviour of hybrid finite volume schemes for advection–diffusion equations: linear and nonlinear approaches," *Numerische Mathematik*, vol. 151, no. 4, pp. 963–1016, 2022.

[11] D. Bessieres, J. Paillol, A. Bourdon, P. Ségur, and E. Marode, "A new one-dimensional moving mesh method applied to the simulation of streamer discharges," *Journal of Physics D: Applied Physics*, vol. 40, no. 21, p. 6559, 2007.

[12] C. Zheng, X. Zhang, Z. Yang, C. Liang, Y. Guo, Y. Wang, and X. Gao, "Numerical simulation of corona discharge and particle transport behavior with the particle space charge effect," *Journal of Aerosol Science*, vol. 118, pp. 22–33, 2018.

[13] J. Jánskỳ and V. P. Pasko, "Modeling of streamer ignition and propagation in the system of two approaching hydrometeors," *Journal of Geophysical Research: Atmospheres*, vol. 125, no. 6, p. e2019JD031337, 2020.

[14] F. Guo, K. Qian, L. Zhang, X. Liu, and H. Peng, "Multiphysics modelling of electroporation under uni-or bipolar nanosecond pulse sequences," *Bioelectrochemistry*, vol. 141, p. 107878, 2021.

[15] R. Herbin, "An error estimate for a finite volume scheme for a diffusion–convection problem on a triangular mesh," *Numerical Methods for Partial Differential Equations*, vol. 11, no. 2, pp. 165–173, 1995.

[16] J. Droniou, "Finite volume schemes for diffusion equations: introduction to and review of modern methods," *Mathematical Models and Methods in Applied Sciences*, vol. 24, no. 08, pp. 1575–1619, 2014.

[17] R. Eymard, T. Gallouët, and R. Herbin, "Finite volume methods," *Handbook of numerical analysis*, vol. 7, pp. 713–1018, 2000.

[18] T. Beale and A. Layton, "On the accuracy of finite difference methods for elliptic problems with interfaces," *Communications in Applied Mathematics and Computational Science*, vol. 1, no. 1, pp. 91–119, 2007.

[19] A. Coco and G. Russo, "Finite-difference ghost-point multigrid methods on Cartesian grids for elliptic problems in arbitrary domains," *Journal of Computational Physics*, vol. 241, pp. 464–501, 2013.

[20] D. Bochkov and F. Gibou, "Solving poisson-type equations with Robin boundary conditions on piecewise smooth interfaces," *Journal of Computational Physics*, vol. 376, pp. 1156–1198, 2019.

[21] J. M. Hyman and M. Shashkov, "Mimetic discretizations for Maxwell's equations," *Journal of Computational Physics*, vol. 151, no. 2, pp. 881–909, 1999.

[22] P. B. Bochev and J. M. Hyman, "Principles of mimetic discretizations of differential operators," in *Compatible spatial discretizations*, pp. 89–119, Springer, 2006.

[23] K. Lipnikov, M. Shashkov, and I. Yotov, "Local flux mimetic finite difference methods," *Numerische Mathematik*, vol. 112, pp. 115–152, 2009.

[24] Y. Coudiere and G. Manzini, "The discrete duality finite volume method for convection-diffusion problems," *SIAM Journal on Numerical Analysis*, vol. 47, no. 6, pp. 4163–4192, 2010.

[25] K. Domelevo and P. Omnes, "A finite volume method for the laplace equation on almost arbitrarytwo-dimensional grids," *ESAIM: Mathematical Modelling and Numerical Analysis*, vol. 39, no. 6, pp. 1203–1249, 2005.

[26] B. Andreianov, F. Boyer, and F. Hubert, "Discrete duality finite volume schemes for leray- lions-type elliptic problems on general 2d meshes," *Numerical Methods for Partial Differential Equations: An International Journal*, vol. 23, no. 1, pp. 145–195, 2007.

[27] X. Blanc, F. Hermeline, E. L. Null, and J. Patela, "Monotonic diamond and ddfv type finite-volume schemes for 2d elliptic problems," *Communications in computational physics*, vol. 34, no. 2, pp. 456–502, 2023.

[28] T. Goudon, S. Krell, and G. Lissoni, "Ddfv method for navier–stokes problem with outflow boundary conditions," *Numerische Mathematik*, vol. 142, no. 1, pp. 55–102, 2019.

[29] T. Goudon, S. Krell, and G. Lissoni, "Convergence study of a ddfv scheme for the navier-stokes equations arising in the domain decomposition setting," in *International Conference on Finite Volumes for Complex Applications*, pp. 335–343, Springer, 2020.

[30] T. Goudon, S. Krell, and G. Lissoni, "Non-overlapping schwarz algorithms for the incompressible navier–stokes equations with ddfv discretizations," *ESAIM: Mathematical Modelling and Numerical Analysis*, vol. 55, no. 4, pp. 1271–1321, 2021.

[31] S. Krell, "Stabilized ddfv schemes for stokes problem with variable viscosity on general 2d meshes," *Numerical Methods for Partial Differential Equations*, vol. 27, no. 6, pp. 1666–1706, 2011.

[32] S. Krell and G. Manzini, "The discrete duality finite volume method for stokes equations on three-dimensional polyhedral meshes," *SIAM Journal on Numerical Analysis*, vol. 50, no. 2, pp. 808–837, 2012.

[33] A. H. Le and P. Omnes, "An a posteriori error estimation for the discrete duality finite volume discretization of the stokes equations," *ESAIM: Mathematical Modelling and Numerical Analysis*, vol. 49, no. 3, pp. 663–693, 2015.

[34] F. Boyer, S. Krell, and F. Nabet, "Inf-sup stability of the discrete duality finite volume method for the 2d stokes problem," *Mathematics of Computation*, vol. 84, no. 296, pp. 2705–2742, 2015.

[35] C. Chainais-Hillairet, S. Krell, and A. Mouton, "Convergence analysis of a ddfv scheme for a system describing miscible fluid flows in porous media," *Numerical Methods for Partial Differential Equations*, vol. 31, no. 3, pp. 723–760, 2015.

[36] C. Cancès, C. Chainais-Hillairet, and S. Krell, "Numerical analysis of a nonlinear free-energy diminishing discrete duality finite volume scheme for convection diffusion equations," *Computational Methods in Applied Mathematics*, vol. 18, no. 3, pp. 407–432, 2018.

[37] G. Lissoni, "DDFV schemes for semiconductors energy-transport models," in *Algoritmy - Conference on Scientific Computing*, 2020.

[38] C. Tayou-Fotso, F. Hubert, and T. Goudon, "Simulation of mixture flows by the discrete duality finite volume method," 2025.

[39] A. Ern and J.-L. Guermond, *Theory and practice of finite elements*, vol. 159. Springer, 2004.

[40] C. Pierre, *Modélisation et simulation de l'activité électrique du coeur dans le thorax, analyse numérique et méthodes de volumes finis.* PhD thesis, Université de Nantes, 2005.

[41] T. Barth and D. Jespersen, "The design and application of upwind schemes on unstructured meshes," in *27th Aerospace sciences meeting*, p. 366, 1989.

[42] E.-H. Quenjel, "Positive scharfetter-gummel finite volume method for convection-diffusion equations on polygonal meshes," 2021.

[43] J. W. Barrett and C. M. Elliott, "Finite element approximation of the dirichlet problem using the boundary penalty method," *Numerische Mathematik*, vol. 49, pp. 343–366, 1986.

[44] B. Maury, "Numerical analysis of a finite element/volume penalty method," *SIAM Journal on Numerical Analysis*, vol. 47, no. 2, pp. 1126–1148, 2009.

[45] J. Droniou, "Non-coercive linear elliptic problems," *Potential Analysis*, vol. 17, no. 2, pp. 181–203, 2002.

[46] J. Droniou and J.-L. Vázquez, "Noncoercive convection–diffusion elliptic problems with neumann boundary conditions," *Calculus of Variations and Partial Differential Equations*, vol. 34, no. 4, pp. 413–434, 2009.

[47] F. Ihlenburg and I. Babuška, "Finite element solution of the helmholtz equation with high wave number part i: The h-version of the fem," *Computers & Mathematics with Applications*, vol. 30, no. 9, pp. 9–37, 1995.

[48] F. Ihlenburg, *Finite element analysis of acoustic scattering*. Springer, 1998.

[49] T. C. Frelet, *Finite element approximation of Helmholtz problems with application to seismic wave propagation*. PhD thesis, INSA de Rouen, 2015.

[50] J. Hyman, M. Shashkov, and S. Steinberg, "The numerical solution of diffusion problems in strongly heterogeneous non-isotropic materials," *Journal of Computational Physics*, vol. 132, no. 1, pp. 130–148, 1997.

[51] R. D. Falgout, J. E. Jones, and U. M. Yang, "The Design and Implementation of hypre, a Library of Parallel High Performance Preconditioners," in *Numerical Solution of Partial Differential Equations on Parallel Computers* (A. M. Bruaset and A. Tveito, eds.), (Berlin, Heidelberg), pp. 267–294, Springer Berlin Heidelberg, 2006.

[52] A. V. Popov and N. Y. Zhu, "Modeling radio wave propagation in tunnels with a vectorial parabolic equation," *IEEE Transactions on Antennas and Propagation*, vol. 48, no. 9, pp. 1403–1412, 2000.

[53] X. Zhang and C. D. Sarris, "Error analysis and comparative study of numerical methods for the parabolic equation applied to tunnel propagation modeling," *IEEE Transactions on Antennas and Propagation*, vol. 63, no. 7, pp. 3025–3034, 2015.